

Automated Quantification of the Resistance of Epithelial Cell Layers from an Impedance Spectrum

Thomas Schmid

Department of Computer Engineering
Universität Leipzig
Leipzig, Germany
schmid@informatik.uni-leipzig.de

Dorothee Günzel

Institute of Clinical Physiology
Charité - Universitätsmedizin Berlin
Berlin, Germany
dorothee.guenzel@charite.de

Martin Bogdan

Department of Computer Engineering
Universität Leipzig
Leipzig, Germany
bogdan@informatik.uni-leipzig.de

Abstract—Quantifying the permeability of intestinal epithelia is a central task in assessing tissue dysfunctions. This can be achieved conveniently by determining the electric resistance of the epithelial tissue by impedance spectroscopy. While in clinical practice this parameter is often estimated by manual extrapolation of discrete two-dimensional plots of impedance spectra, this approach is known to be particularly unprecise for spectra that deviate from a semicircular shape. Previous computational approaches achieved less than ten percent deviation from the known target value on average, but outliers exhibited significantly larger maximum deviations. Here, we show that systematic feature extraction and selection allow estimation of the epithelial resistance with less than one percent deviation from the known target value on average and less than ten percent at maximum. As a result of detailed modeling of cell culture lines and functional states, epithelial resistance for the cell lines HT-29/B6, IPEC-J2 and MDCK I can be quantified reliably under control conditions, as well as under influence of EGTA and nystatin.

Keywords—Physiology; Epithelia; Impedance Spectroscopy; Feature Selection; Artificial Neural Networks; Random Forests.

I. INTRODUCTION

Intestinal epithelial cells form the primary barrier of the gut between the body's interior and the exterior environment (i.e., the gut contents). In general, all epithelial and endothelial cells are connected by arrays of transmembrane proteins, called tight junctions that seal the space between two neighbouring cells. Tight junction properties are determined by their major constituents, the members of the claudin protein family. While certain claudins strengthen the barrier function (e.g., claudin-1 in skin, claudin-5 in the blood-brain barrier [1]), others convey specific charge and/or size selectivity [1][2]. Regulation and dysregulation of these channel-forming claudins appear to be paramount in the pathophysiology of numerous diseases [3].

As a whole, the epithelium regulates transport of molecules and establishes a tight barrier against toxins and pathogens. The permeability of epithelial tissue to ions is reflected by its electric resistance, called transepithelial resistance (R^T , often also abbreviated as TER). R^T is the sum of the subepithelial resistance R^{sub} and the epithelial resistance R^{epi} . These partial resistances are individual and independent parameters of the tissue, and exact knowledge of their values is crucial in the analysis of epithelial dysfunctions. For patients with inflammatory intestinal diseases, e.g, it was observed that due to the inflammation R^{sub} increased whereas R^{epi} decreased.

The most common way to assess tissue permeability is a direct measurement of fluxes, e.g., by using radioactive isotopes or labelled substances. Alternatively, permeability of the two major extracellular ion species, Na^+ and Cl^- , is determined by measuring tissue conductance or its reciprocal, resistance, e.g., by using "chopstick electrodes" or Ussing chambers [4]. A more convenient way to assess tissue permeability is impedance spectroscopy. Typically, up to 50 complex-valued impedances Z are obtained by measuring current-voltage relationships under alternate current (AC) with varying frequencies [5]. A common representation of these measurements are Nyquist diagrams, where the real part $\Re(Z)$ of an impedance is plotted against the imaginary part $\Im(Z)$ (Figure 1). To analyze samples, an equivalent electric circuit of appropriate complexity is modeled [6]. The simplest circuit that incorporates R^{epi} is a resistor-capacitor (RC) circuit (Figure 2a). To represent physiological polarity of epithelial cells, a circuit with two RC subcircuits in series and a resistor in parallel may be used (Figure 2b). In both cases, the subepithelium can be represented by a further resistor in series.

In contrast to DC resistance measurements, impedance spectroscopy allows to distinguish between R^{sub} and R^{epi} . Under in vivo conditions the subepithelium does not contribute

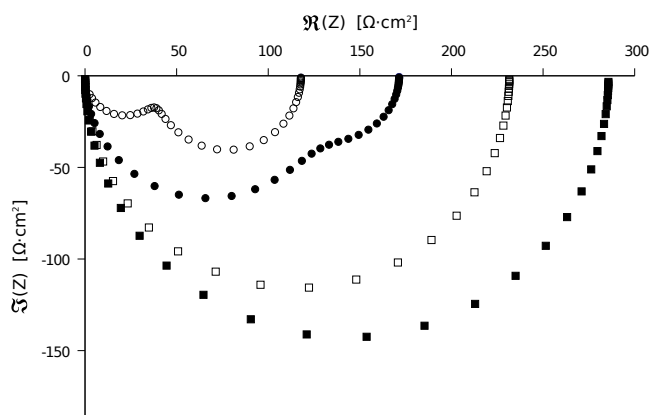


Figure 1. Overlay of two semi- and two non-semicircular impedance spectra with 42 frequencies where real (\Re) and imaginary (\Im) part of each complex-valued impedance Z are plotted against each other.

to the barrier function as subepithelial capillaries are in close contact with the basolateral membrane of the epithelial cells. Further, impedances reflect not only conductive but also capacitive properties and allow to derive the epithelial capacitance which directly depends on the epithelial surface area [7].

In previous work, we have demonstrated that traditional ways to estimate R^{epi} from an impedance spectrum, e.g. visual extrapolation, can lead to serious errors in analysis of epithelial characteristics. We have also demonstrated that estimations can be improved by applying machine learning techniques on complex-valued impedances of error-prone [8] or on extracted features of ideal impedance spectra, respectively [9]. We have introduced detailed and realistic models of the electric behavior of three epithelial cell lines [10]: the human colon carcinoma cell line HT-29/B6, the porcine jejunum cell line IPEC-J2 and the canine kidney cell line MDCK I under control conditions, as well as under influence of EGTA, nystatin or both. Rationale behind these models is that for a given electric circuit, the theoretical impedance at a given frequency can be calculated if the values of all circuit components are given.

Here, we combine systematic modeling of impedance spectra with systematic feature extraction in order to improve quantification of R^{epi} . We show that employing a mixture of both measured and extracted features reduces relative deviation from the target value when applying supervised learning techniques like random forests. Compared with previous approaches, the estimation error is significantly reduced.

II. METHODS

A. Modeling Impedance Spectra

For all three modeled cell lines, an equivalent circuit consisting of two RC subcircuits a (R_a, C_a) and b (R_b, C_b) located in series and a resistor in parallel (R_p) is assumed (Figure 2). In accordance with Kirchhoff's laws, the corresponding impedance Z at an angular frequency ω can be derived from the impedances of the circuit components:

$$Z(\omega) = \frac{R_p(R_a + R_b) + i\omega[R_p(R_a\tau_b + R_b\tau_a)]}{R_a + R_b + R_p(1 - \omega^2\tau_a\tau_b) + i\omega[R_p(\tau_a + \tau_b) + R_a\tau_b + R_b\tau_a]} \quad (1)$$

where $i = \sqrt{-1}$, and $\tau_a = R_a C_a$ and $\tau_b = R_b C_b$.

In the measurements to be modeled, ten frequencies per decade are used. Based on a lowest frequency f_1 of 1.3 Hz,

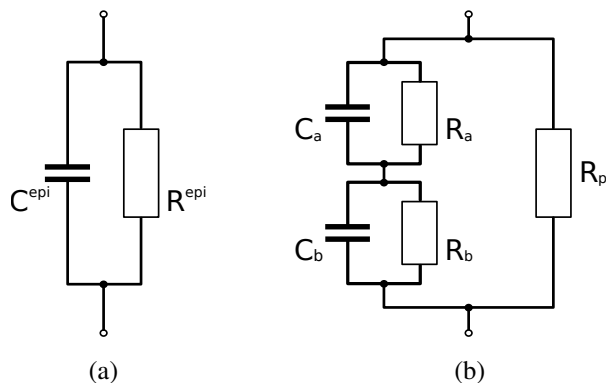


Figure 2. Equivalent circuits. (a) A simple resistor-capacitor (RC) circuit yields semicircular impedance spectra. (b) A 2-RC circuit yields semicircular or non-semicircular impedance spectra.

higher frequencies f_i with $1 < i \leq n = 42$ are multiples by a factor of $10^{0.1}$ (~ 1.26). Note that the value of f_1 is chosen to avoid obtaining multiples of 50 Hz (mains frequency) and that for application with Eq. 1, $\omega_i = 2\pi/f_i$ is calculated.

Further, we model and apply synthetic data scatter reflecting deviations from the theoretical impedance value caused by the electrophysiological measurement set-up. This scatter is here modeled based on relative deviations of real part \Re and imaginary part \Im of measured impedances from theoretical values. For a given impedance Z at frequency $f = 2\pi\omega$, relative deviation σ of $\Re(Z)$ is approximated as second-order Fourier series ($n=2$) and relative deviations of $\Im(Z)$ is approximated as fourth-order polynomial function ($n=4$):

$$\sigma_{\Re}(f) = a_0 + \sum_{i=1}^n a_i \cdot \cos(n\omega f) + b_i \cdot \sin(n\omega f) \quad (2)$$

$$\sigma_{\Im}(f) = a_0 + \sum_{i=1}^n a_i \cdot f^i \quad (3)$$

where coefficients w , a_0 , a_1 , b_1 , a_2 , b_2 or a_0 , a_1 , a_2 , a_3 , a_4 respectively were determined by function fitting and a_0 is modeled as dependent on R^T . For further details and comparison with measured data, see [8] or [10].

For all synthetic samples used in the following, first complex impedances are calculated according to model parameters. Then data scatter is added, and finally, polar impedances are calculated from the scattered complex impedances.

B. Sampling Cell Lines and Functional States

While IPEC-J2 and MDCK I cells typically show relatively high R^T values under physiological conditions, for HT-29/B6 cells relatively low values are measured. Based on these findings, as well as on further published measurement results, parameter ranges of the components of the equivalent circuit were defined and confirmed in previous work [10]. By extending this modeling approach for individual or combined application of EGTA and nystatin, impedance spectra for a total of 11 measurement scenarios are synthesized; note that for MDCK I cells, only measurements for Control, nystatin and EGTA were available for modeling [10]. Randomized samples of each scenario are combined to a data set of 275,000 samples (Tab. I), which is then split into a training set of 200,000 and a test set of 75,000 samples.

C. Reference Methods to Quantify Epithelial Resistance

Reliability of the hereby introduced approach was compared to a conventional approach to estimate R^{epi} , as well as to two approaches that we have proposed in previous work.

TABLE I. SAMPLE SIZES FOR MODELED EPITHELIAL CELL LINES AND THEIR FUNCTIONAL CONDITIONS.

Condition	HT-29/B6	IPEC-J2	MDCK I
Control	25.000	25.000	25.000
Nystatin	25.000	25.000	25.000
EGTA	25.000	25.000	25.000
EGTA+nystatin	25.000	25.000	—

1) *Frequency-blind Circle Fit (Method M1)*: Each impedance spectrum was regarded as Nyquist diagram and a Cole-Cole fit [11] was applied, i.e., a circle was fitted as described by Kasa [12]. For this task, the *R* package *conicfit* and its function *CircleFitByKasa* was used. The intercept with the x-axis at the low frequency end was taken as R^{epi} .

2) *Neural Network Prediction (Method M2)*: Complex-valued impedances Z_1, \dots, Z_{10} of the first decade of frequencies (f_1, \dots, f_{10}) were used to train an artificial neural network. This implies a 20-dimensional input feature space I :

$$I_{M2} = \{\Re(Z_1), \dots, \Re(Z_{10}), \Im(Z_1), \dots, \Im(Z_{10})\} \quad (4)$$

While this approach follows a method previously published by us [8], we improved the precision of predictions by using the Rprop algorithm [13] instead of conventional backpropagation. Employed Rprop parameters were $\eta^+ = 1.2$, $\eta^- = 1.2$, $\Delta_{max} = 50.0$, $\Delta_{min} = 0.000001$ and $\Delta_0 = 0.07$. We used the *Fast Artificial Neural Network* library [14] to perform automated evaluation of 30 feed-forward networks with one hidden layer and $n \in \{1, \dots, 30\}$ hidden neurons (20- n -1 architecture). Training these networks in parallel with the same data, the architecture 20-9-1 was identified as best performer and used for predictions.

3) *Magnitude at 1.3 Hz (Method M3)*: In previous evaluations of features for prediction of R^{epi} from an impedance spectrum, we found that the magnitude r observed at 1.3 Hz is a reliable approximation for semicircular spectra [9]. While reliability decreases with non-semicircular spectra, this one-feature approach is ultimately easy to implement and a feasible method for comparison. For a given spectrum, we simply used the value of $r(Z_1) \in S_r$ as prediction for R^{epi} .

D. Feature Extraction-based Approach

To improve prediction of R^{epi} from impedance spectra, we suggest a supervised learning approach that uses systematic feature extraction and selection. After extracting implicit features for each spectrum, we ranked explicit and implicit features. Finally, subsets of these features were assessed by applying supervised learning.

From calculations, $n=42$ tuples of real and imaginary parts ($(\Re(\omega_0), \Im(\omega_0)), \dots, (\Re(\omega_{n-1}), \Im(\omega_{n-1}))$), are obtained. Real and imaginary parts of a spectrum can be regarded as separate feature sets S_{\Re} and S_{\Im} :

$$S_{\Re} = \{\Re(\omega_0), \dots, \Re(\omega_{n-1})\} \quad (5)$$

$$S_{\Im} = \{\Im(\omega_0), \dots, \Im(\omega_{n-1})\} \quad (6)$$

As an alternative representation, these complex values were transformed into polar coordinates, i.e., into phase angle ϕ and magnitude r . This resulted in two alternative sets S_{ϕ} and S_r :

$$S_{\phi} = \{\phi(\omega_0), \dots, \phi(\omega_{n-1})\} \quad (7)$$

$$S_r = \{r(\omega_0), \dots, r(\omega_{n-1})\} \quad (8)$$

1) *Feature Extraction*: Based on the features that can be explicitly measured or synthesized, respectively, a set I_e of explicit input features was defined:

$$I_e = S_{\Re} \times S_{\Im} \times S_{\phi} \times S_r \quad (9)$$

where S_{\Re} , S_{\Im} , S_{ϕ} and S_r contained $n=42$ features each.

Additionally, the development of magnitude and phase over time was represented in sets of differential features:

$$S_{\Delta\phi} = \{\Delta\phi | \Delta\phi_i = \phi(\omega_{i+1}) - \phi(\omega_i), 0 \leq i < n-1\} \quad (10)$$

$$S_{\Delta r} = \{\Delta r | \Delta r_i = r(\omega_{i+1}) - r(\omega_i), 0 \leq i < n-1\} \quad (11)$$

which are combined to a set I_d of differential input features:

$$I_d = S_{\Delta\phi} \times S_{\Delta r} \quad (12)$$

where $S_{\Delta\phi}$ and $S_{\Delta r}$ contained $n=41$ features each.

Further, a total of 16 statistical properties like minimum, maximum and range were determined for each feature set (for details see appendix).

$$G_{\Re} = \{x | x \hat{=} \text{statistical property of } S_{\Re}\} \quad (13)$$

$$G_{\Im} = \{x | x \hat{=} \text{statistical property of } S_{\Im}\} \quad (14)$$

$$G_{\phi} = \{x | x \hat{=} \text{statistical property of } S_{\phi}\} \quad (15)$$

$$G_r = \{x | x \hat{=} \text{statistical property of } S_r\} \quad (16)$$

$$G_{\Delta\phi} = \{x | x \hat{=} \text{statistical property of } S_{\Delta\phi}\} \quad (17)$$

$$G_{\Delta r} = \{x | x \hat{=} \text{statistical property of } S_{\Delta r}\} \quad (18)$$

which were combined to a set I_i of implicit input features:

$$I_i = G_{\Re} \times G_{\Im} \times G_{\phi} \times G_r \times G_{\Delta\phi} \times G_{\Delta r} \quad (19)$$

By combining explicit, differential and implicit features, an 346-dimensional input feature space I was obtained that represents 42 measured impedances:

$$I = I_e \times I_d \times I_i \quad (20)$$

2) *Feature Selection*: Three alternative feature selection approaches were employed and assessed:

- Filter-based approach. We applied Correlation-based Feature Selection (CFS) on the input space I of the 200,000 training samples. For this task, the *R* package *FSelector* and its function *cfs* was used. In contrast to other multivariate filters, CFS evaluates feature subsets instead of single features [15]. In particular, CFS returns not a ranking of features but a fixed subset of features. Here, CFS evaluated a one-dimensional subset best that consists only of the range of S_r .
- Expert knowledge-based approach (EXP). As a matter of theory, low-frequency impedances are closely related to R^{epi} [6]. Also, the magnitude of an impedance is more meaningful than other representations. Therefore, we manually selected the feature sets G_r and $G_{\Delta r}$, as well as magnitudes of the low-frequency impedances Z_1, \dots, Z_5 and related differences ($r(Z_{i+1}) - r(Z_i)$). This yielded a 42-dimensional representation.
- Wrapper-based approach (RF₈₄). Variable importance was assessed for the input space I of the 200,000 training samples. Using the *R* package *randomForest*, a random forest (RF) consisting of 500 trees was trained to predict R^{epi} and used in a wrapper-like way. After training, variable importance values were used to rank the input features, and a subset of 84 top-ranked features was chosen as representation of an impedance spectrum. This number of selected features is simply motivated by the initial number of 84 features per spectrum. Automated wrapper techniques like sequential feature selection or recursive feature elimination were omitted here due to the high computational costs.

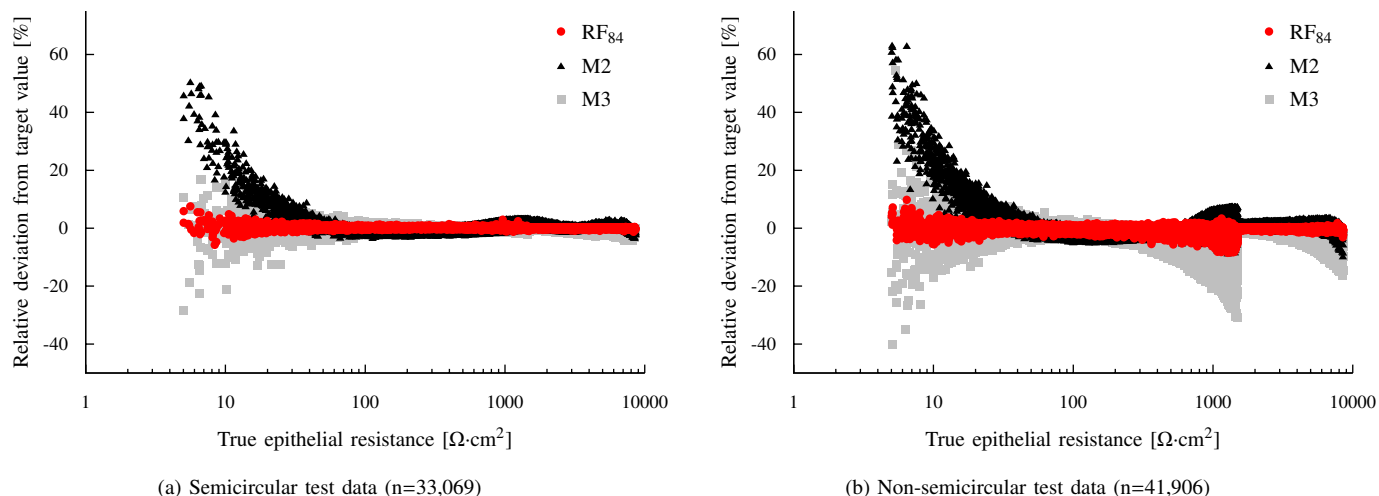


Figure 3. Relative deviations of estimated values from true R^{epi} . Deviations achieved by the feature extraction-based approach RF_{84} , as well as for the two best performing reference methods (M2, M3) are plotted against the respective true target value. Values shown refer either to (a) semicircular or (b) nonsemicircular spectra, which are discriminated by the relation between apical and basolateral time constants.

3) *Evaluation*: All three feature selection approaches CFS, EXP and RF_{84} were used to estimate R^{epi} for the 75,000 samples of the test data. Deviations of the obtained estimations from the target were compared to reference methods M1, M2 and M3.

III. RESULTS

The reliability of estimations for R^{epi} was assessed. For each approach, the relative deviation of an predicted value t_p from the target value t , or error Δt respectively, was used:

$$\Delta t = \frac{t_p - t}{t} \quad (21)$$

Based on Δt , both absolute-valued deviations, as well as signed deviations were analyzed.

A. Absolute-valued Deviations

Assessing absolute-valued relative deviation from the target $|\Delta t|$, for reference methods, as well as feature extraction-based approaches a mean deviation of less than $\pm 2.0\%$ was observed. Maximum deviations, however, laid between $\pm 54.4\%$ and $\pm 92.1\%$ for the reference methods and between $\pm 9.8\%$ and $\pm 85.9\%$ for feature extraction-based approaches. Maximum deviations for the 84- and 20-dimensional cartesian representations M1 and M2 were comparable to maximum deviations of the two one-dimensional polar representations M3 and CFS. The mixed 42- and mixed 84-dimensional representations learned by random forests both showed significantly lower maximum deviations. Lowest mean and maximum deviations of all methods assessed were obtained by the random forest trained with the 84 top-ranked features. Figure 4 shows boxplots of $|\Delta t|$ for all methods evaluated.

B. Estimations for Semi- and Non-semicircular Spectra

Deviations of the random forest trained with the 84 top-ranked features (RF_{84}) were further assessed by separating semicircular and non-semicircular spectra of the 75,000 test samples. In continuity with our previous work [7], spectra from equivalent circuits with $\tau_a \leq 5 \cdot \tau_b$ or $\tau_b \leq 5 \cdot \tau_a$ were considered

as semicircular spectra; all spectra with greater difference between τ_a and τ_b were considered as non-semicircular.

As Figure 3 illustrates, estimations by reference methods M2 and M3 tended to become unprecise with low values of R^{epi} ; this held true for both semi- and non-semicircular spectra. Using the feature extraction-based approach RF_{84} , deviations for high and low target values laid below 10% and thereby in a significantly smaller range than for M2 and M3.

For semicircular spectra with larger target values (Figure 3a), deviations of estimations by the feature extraction-based approach RF_{84} laid in a range comparable to M2 and M3. For non-semicircular spectra with larger target values (Figure 3b), RF_{84} showed in most cases small improvements over M2; using method M3 appeared to induce systematic error that causes greater deviations than for M2 and RF_{84} .

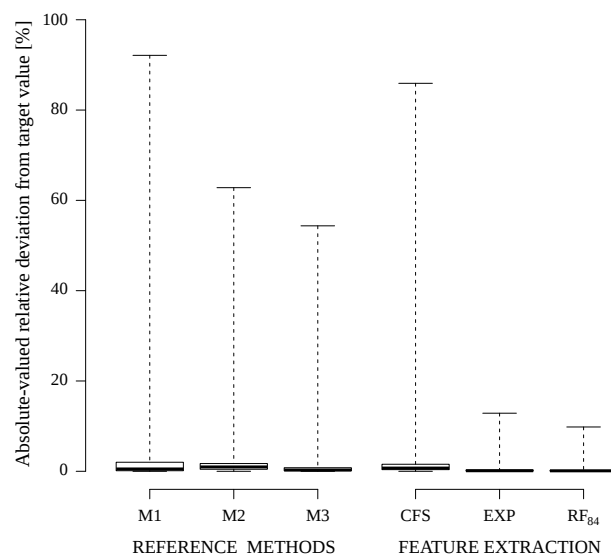


Figure 4. Boxplots of absolute-valued relative deviations from true values of R^{epi} [$\pm\%$]. Each box reflects median, 1. and 3. quartile.

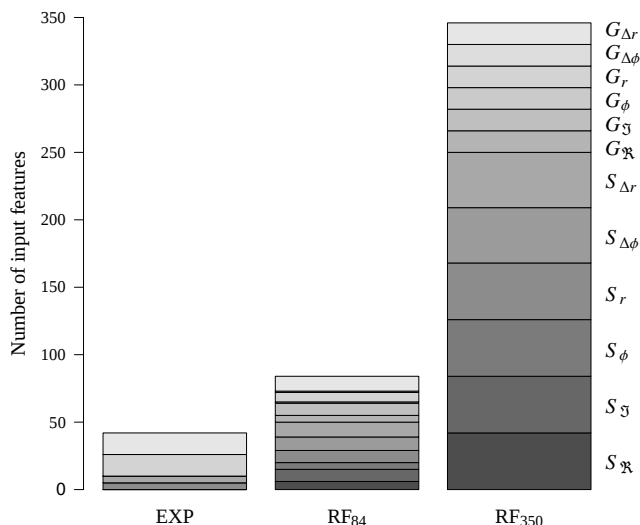


Figure 5. Usage of feature subsets. The approaches RF_{84} and RF_{350} use features from all subsets, EXP only from the subsets S_r , $S_{\Delta r}$, G_r and $G_{\Delta r}$.

IV. DISCUSSION

A. Comparison of Problem Representations

Evaluation of the test samples showed that the filter-based (CFS), as well as the expert-based (EXP) and wrapper-based subset (RF_{84}) yielded estimations with little average deviation from the target. While using the one-dimensional CFS representation exhibits similar maximum error as reference methods, EXP and RF_{84} allowed for significantly lower maximum error than the reference methods. Yet, the features used in both approaches exhibited different characteristics (Figure 5). EXP employed only features of direct physical relevance and only half as many dimensions as RF_{84} . RF_{84} on the other hand employed more features, but reduced the maximum error to a level comparable to a much more high-dimensional representation of 350 features (Tab. II).

B. Use of Random Forests

Exploiting the variable importance determined by random forests allowed to efficiently combine supervised learning with a wrapper-based feature selection. As in previous studies [16], the ranking of all 350 features by a random forests could be used to identify features appropriate for the given task. In particular, top-ranked features yielded estimations with lesser deviations than a feature set determined by filter-based CFS.

TABLE II. RELATIVE DEVIATIONS FROM R^{EPI} [$\pm\%$].

	EXP	RF_{84}	RF_{350}
Maximum	12.9	9.81	9.24
3. Quartile	0.30	0.23	0.25
Mean	0.29	0.22	0.23
Median	0.12	0.10	0.11
1. Quartile	0.05	0.04	0.05
Minimum	0.00	0.00	0.00

Compared with the previously developed ANN approach (M2), the random forest approaches EXP and RF_{84} performed with similar precision for samples with large target values and with much better precision for small target values ($R^{epi} < 25 \Omega\text{cm}^2$). This is in accordance with findings in previous comparisons of random forests with ANNs [16]. As a result, both EXP and RF_{84} allowed for the first time reliable estimations for impedance spectra reflecting epithelia with low R^{epi} .

C. Limitations

The feature extraction-based approach suggested here to estimate R^{epi} work equally well for cell types and conditions where time constants of the apical and basolateral cell membranes are similar (as usually found in cell culture) as for conditions where these time constants differ considerably (as found in many tissues). Moreover, Figure 3 illustrates that reliable quantification of R^{epi} from an impedance spectrum is feasible for resistance values spanning several orders of magnitude. As the presented method involves modeled spectra, however, applicability is naturally depending on modeling and sampling of the data. The previously modeled data that is used here is in good accordance with measured data [10]. While a variety of cell lines and functional states is considered, results and estimations obtained here are still limited to the scenarios modeled. Also, characteristics of the training and test data influence characteristics of estimation methods. For example, precision of supervised learning methods tends to decrease if the number of samples decreases. To this end, e.g., the density of target values needs to be considered (cf. Figure 6).

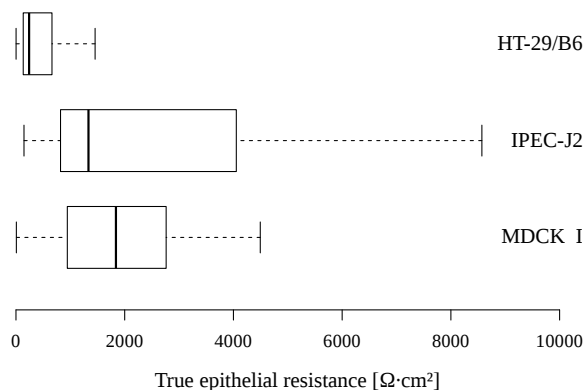


Figure 6. R^{epi} target values [$\Omega\cdot\text{cm}^2$] of the test data ($n=75,000$) grouped by cell lines. Each box reflects median, 1. and 3 quartile.

D. Relevance for Biomedical Applications

Impedance spectroscopic techniques are increasingly gaining importance in biomedical applications like monitoring growth of cultured epithelial and endothelial cells (e.g., retinal pigment epithelium, gastrointestinal tract cells, pulmonary cells, blood-brain-barrier models [17][18]), or alterations of barrier function during pharmacological studies [19][20][17]. Furthermore, impedance spectroscopy is the only technique that allows functional distinction between epithelial and subepithelial properties of ex vivo tissue, such as intestinal biopsies of patients with suspected barrier impairment.

If the technique is to be used on a routine basis, however, reliable automatization for the evaluation of impedance spectra is indispensable. On one hand, manual evaluation of impedance spectra to extract the physiologically relevant parameter, R^{epi} , requires extensive user training and is time consuming, as individual spectra need to be fitted by complex equations [9]. On the other hand, currently available systems usually only record R^T (i.e., the sum of the subepithelial and epithelial resistance) or even only relative alterations in R^T over the time-course of an experiment, as estimation of absolute R^T values is too error-prone [21][17].

V. CONCLUSIONS

While impedance spectroscopy is a convenient measurement technique, determining the resistance of an epithelial tissue with traditional approaches is error-prone under certain circumstances. Here, we have shown that this clinically important parameter can be quantified with high precision by training random forests with features extracted from modeled impedance spectra. In particular, we have shown that this approach outperforms both traditional estimation techniques and a state-of-the-art artificial neural network approach. Due to detailed and realistic modeling, we suggest this approach is valid for the epithelial cell lines HT-29/B6, IPEC-J2 and MDCK I under control conditions, as well as under the influence of nystatin and EGTA.

APPENDIX

For the explicit feature sets $S_{\mathfrak{R}}$, $S_{\mathfrak{G}}$, S_{ϕ} and S_r , as well as for the differential feature sets $S_{\Delta\phi}$ and $S_{\Delta r}$ a total of 16 statistical features (Tab. III) was calculated. By combining these statistical features of set S , a novel set G of related global features was extracted.

TABLE III. STATISTICAL FEATURES FOR FEATURE SET $S_{\mathfrak{R}}$.

Feature	Definition with $x_i \in S_{\mathfrak{R}}$ and $n = \#(S_{\mathfrak{R}})$	Description
$\min(S_{\mathfrak{R}})$	$\{x : x \leq x_i \ \forall x_i \in S_{\mathfrak{R}}\}$	Minimum
$\max(S_{\mathfrak{R}})$	$\{x : x_i \leq x \ \forall x_i \in S_{\mathfrak{R}}\}$	Maximum
$R(S_{\mathfrak{R}})$	$\max(S_{\mathfrak{R}}) - \min(S_{\mathfrak{R}})$	Range
$P_{0,1}(S_{\mathfrak{R}}^*)$	$x_{[0,1-n+1]}$	1. Percentile
$Q_{0,25}(S_{\mathfrak{R}}^*)$	$x_{[0,25-n+1]}$	1. Quartile
$Q_{0,75}(S_{\mathfrak{R}}^*)$	$x_{[0,75-n+1]}$	3. Quartile
$P_{0,9}(S_{\mathfrak{R}}^*)$	$x_{[0,9-n+1]}$	9. Percentile
$R_{IQ}(S_{\mathfrak{R}})$	$Q_{0,75}(S_{\mathfrak{R}}^*) - Q_{0,25}(S_{\mathfrak{R}}^*)$	Interquartile distance
$R_{IP}(S_{\mathfrak{R}})$	$Q_{0,9}(S_{\mathfrak{R}}^*) - Q_{0,1}(S_{\mathfrak{R}}^*)$	Interpercentile distance
$\bar{x}_{med}(S_{\mathfrak{R}}^*)$	$\begin{cases} x_{(\frac{n+1}{2})}, & \text{if } n \text{ odd} \\ \frac{1}{2}(x_{(\frac{n}{2})} + x_{(\frac{n}{2}+1)}), & \text{if } n \text{ even} \end{cases}$	Median
$\bar{x}_{arithm}(S_{\mathfrak{R}})$	$\frac{1}{n} \sum_{i=1}^n x_i$	Arithmetic mean
$\bar{x}_{geom}(S_{\mathfrak{R}})$	$\sqrt[n]{\prod_{i=1}^n x_i}$	Geometric mean
$\bar{x}_{harm}(S_{\mathfrak{R}})$	$\frac{n}{\sum_{i=1}^n \frac{1}{x_i}}$	Harmonic mean
$s^2(S_{\mathfrak{R}})$	$\frac{1}{n-1} \sum_{i=1}^n (x_i - \bar{x}_{arithm}(S_{\mathfrak{R}}))^2$	Variance
$s(S_{\mathfrak{R}})$	$\sqrt{s^2(S_{\mathfrak{R}})}$	Standard deviation
$R_{MM}(S_{\mathfrak{R}})$	$\bar{x}_{med}(S_{\mathfrak{R}}) - \bar{x}_{arithm}(S_{\mathfrak{R}})$	Distance between median and arithmetic mean

REFERENCES

- [1] D. Günzel and A. S. L. Yu, "Claudins and the modulation of tight junction permeability," *Physiological Reviews*, vol. 93, no. 2, 2013, pp. 525–569.
- [2] S. M. Krug et al., "Charge-selective claudin channels," *Annals of the New York Academy of Sciences*, vol. 1257, 2012, pp. 20–28.
- [3] S. M. Krug, J.-D. Schulzke, and M. Fromm, "Tight junction, selective permeability, and related diseases," *Seminars in Cell & Developmental Biology*, vol. 36, 2014, pp. 166–176.
- [4] B. Jovov, N. Wills, and S. Lewis, "A spectroscopic method for assessing confluence of epithelial cell cultures," *American Journal of Physiology*, vol. 261, no. 6 Pt 1, 1991, pp. C1196–203.
- [5] J. R. Macdonald and W. B. Johnson, *Fundamentals of Impedance Spectroscopy*. John Wiley & Sons, Inc., 2005, pp. 1–26.
- [6] D. Günzel et al., "From TER to trans- and paracellular resistance: lessons from impedance spectroscopy," *Annals of the New York Academy of Sciences*, vol. 1257, no. 1, 2012, pp. 142–151.
- [7] T. Schmid, D. Günzel, and M. Bogdan, "Automated quantification of the capacitance of epithelial cell layers from an impedance spectrum," in *Proceedings of the 7th International Conference on Bioinformatics, Biocomputational Systems and Biotechnologies*, 2015, pp. 27–32.
- [8] T. Schmid, M. Bogdan, and D. Günzel, "Discerning apical and basolateral properties of HT-29/B6 and IPEC-J2 cell layers by impedance spectroscopy, mathematical modeling and machine learning," *PLOS ONE*, vol. 8, no. 7, 2013, p. e62913.
- [9] T. Schmid, D. Günzel, and M. Bogdan, "Efficient prediction of x-axis intercepts of discrete impedance spectra," in *Proceedings of the 21st European Symposium on Artificial Neural Networks, Computational Intelligence and Machine Learning (ESANN)*, 2013, pp. 185–190.
- [10] T. Schmid, "Automatisierte Analyse von Impedanzspektren mittels konstruktivistischen maschinellen Lernens," Ph.D. dissertation, Universität Leipzig, Germany, 2018.
- [11] K. S. Cole and R. H. Cole, "Dispersion and absorption in dielectrics I. alternating current characteristics," *The Journal of Chemical Physics*, vol. 9, no. 4, 1941, pp. 341–351.
- [12] I. Kasa, "A circle fitting procedure and its error analysis," *IEEE Transactions on Instrumentation and Measurement*, vol. 1001, no. 1, 1976, pp. 8–14.
- [13] M. Riedmiller and H. Braun, "A direct adaptive method for faster backpropagation learning: the RPROP algorithm," *IEEE International Conference on Neural Networks*, 1993, pp. 586–591.
- [14] S. Nissen, "Implementation of a fast artificial neural network library," University of Copenhagen, Denmark, Tech. Rep., 2003.
- [15] M. A. Hall, "Correlation-based feature selection for machine learning," Ph.D. dissertation, University of Waikato, New Zealand, 1999.
- [16] T. Schmid, D. Günzel, and M. Bogdan, "Automated quantification of the relation between resistor-capacitor subcircuits from an impedance spectrum," in *Proceedings of the International Conference on Bio-Inspired Systems and Signal Processing*, 2014, pp. 141–148.
- [17] B. Srinivasan et al., "TEER measurement techniques for in vitro barrier model systems," *Journal of Laboratory Automation*, vol. 20, no. 2, 2015, pp. 107–126.
- [18] N. Onnela et al., "Electric impedance of human embryonic stem cell-derived retinal pigment epithelium," *Medical & Biological Engineering & Computing*, vol. 50, no. 2, 2012, pp. 107–116.
- [19] F. A. Atienzar, H. Gerets, K. Tilmant, G. Toussaint, and S. Dhalluin, "Evaluation of impedance-based label-free technology as a tool for pharmacology and toxicology investigations," *Biosensors*, vol. 3, no. 1, 2013, pp. 132–156.
- [20] S. Ramasamy, D. Bennet, and S. Kim, "Drug and bioactive molecule screening based on a bioelectrical impedance cell culture platform," *International Journal of Nanomedicine*, vol. 9, no. 1, 2014, pp. 5789–5809.
- [21] Z. Maheraly et al., "Real-time acquisition of transendothelial electrical resistance in an all-human, in vitro, 3-dimensional, bloodbrain barrier model exemplifies tight-junction integrity," *The FASEB Journal*, vol. 32, no. 1, 2018, pp. 168–182.